About Objective 3-D Analysis of Airway Geometry in Computerized Tomography

Oliver Weinheimer*, *Member, IEEE*, Tobias Achenbach, Carsten Bletz, Christoph Düber, Hans-Ulrich Kauczor, and Claus Peter Heussel

***Abstract*—The technology of multislice X-ray computed tomography (MSCT) provides volume data sets with approximately isotropic resolution, which permits a noninvasive 3-D measurement and quantification of airway geometry. In different diseases, like emphysema, chronic obstructive pulmonary disease (COPD), or cystic fribrosis, changes in lung parenchyma are associated with an increase in airway wall thickness. In this paper, we describe an objective measuring method of the airway geometry in the 3-D space. The limited spatial resolution of clinical CT scanners in comparison to thin structures like airway walls causes difficulties in the measurement of the density and the thickness of these structures. Initially, these difficulties will be addressed and then a new method is introduced to circumvent the problems. Therefore the wall thickness is approximated by an integral based closed-form solution, based on the volume conservation property of convolution. We evaluated the method with a phantom containing 10 silicone tubes and proved the repeatability in datasets of eight pigs scanned twice. Furthermore, a comparison of CT datasets of 16 smokers and 15 nonsmokers was done. Further medical studies are ongoing.**

***Index Terms*—Airway geometry measurement, closed-form solution for the measurement of thin structures in computed tomography (CT), measurement of thin structures, quantitative computed tomography (CT).**

I. Introduction

COMPUTED tomography (CT) is currently the method of choice for noninvasive and sensitive imaging of pathologic changes of the lung. Development of multislice X-ray computed tomography (MSCT) combines the advantages of the high-resolution CT (HRCT) and spiral CT and permits visualization of the lungs and the bronchial tree up to the subsegmental level.

There were several manual, semiautomatic, and automatic methods presented in the past for measuring the airway geometry in different kinds of CT images [1]–[7].

Study [6] is an example for a manual measurement method. Two observers independently analyzed the images using a defined window-level setting for the applied Hounsfield window. The CT scans were scored according to diagnostic criteria available in the literature [8], [9].

The algorithm applied in [3] is based on the full-width at half-maximum (FWHM) method, which means it is assumed that the airway wall starts in the middle of maximum and minimum of the X-ray density on a virtual ray (density profile, see e.g., Fig. 1) from the airway center to the wall.

The method used in [2] determines the lumen by a seeding algorithm. A circle is drawn around the airway and is iteratively eroded until the outer border of the airway is identified.

In [5], a model-based method is proposed. The scanner is modeled by its 3-D point spread function (PSF) described by a 3-D Gaussian with standard deviations in x, y, and z directions. The bronchus is modeled as a circular tube. The difference between the modeled, artificial image and the actual, real CT image is minimized. A tilt angle compensation is applied to the 2-D measurement results. The method was validated using a plexiglas phantom containing five plexiglas tubes with wall thicknesses between 1.16 and 3.05 mm. The range of the inner diameters was 0.98 mm to 6.5 mm.

In [7], a cost function is used and the true inner edges of bronchi are searched by dynamically maximizing the cost function, which is a weighted function depending on the first and the second derivative. They validated the method with a plexiglas phantom containing seven plexiglas tubes with inner diameters between 0.98 and 19.25 mm. Only six tubes with known inner diameters ranging from 1.98 to 19.25 mm were used for validation since the method could not resolve the smallest 0.98 mm inner diameter tube, so the smallest tube was excluded and the analysis was based on the remaining six tubes.

In [10] two initial tubes are fitted along the inner and outer airway wall based on the image gradients. Global tree analysis is also performed. No phantom measurements are reported, so it is difficult to estimate the precision of this method.

To summarize the conclusions of these papers, "an accurate, repeatable airway geometry measurement cannot be made using manual-tracing techniques" [1]. Finding the true edges of small objects in CT images is a complex problem; FWHM leads to unacceptable errors. In this paper, we describe the theory of measurement of thin structures in CT in general. Additionally, a new method based on an integral calculus for the measurement of thin structures in CT will be introduced. The wall thickness is approximated in this method by an integral based closed-form solution. Hence, the method can be implemented in an efficient computational form, because no minimization or maximization problem has to be solved. The new method was validated by using an artificial phantom containing 10 silicone tubes of wall thicknesses between 0.3 and 2.5 mm and inner diameters be-

Manuscript received May 9, 2007; revised June 7, 2007. This work was supported in part by AstraZeneca, in part by the Mainzer Forschungsförderungsprogramm (MAIFOR), and in part by the Deutsche Forschungsgemeinschaft (DFG-FOR474). *Asterisk indicates corresponding author*.

*O. Weinheimer is with the Institute of Computer Science, Johannes Gutenberg-University, 55099 Mainz, Germany and also with the Department of Radiology, Johannes Gutenberg-University of Mainz, 55101 Mainz, Germany (e-mail: mail@oliwe.com).

T. Achenbach, C. Bletz, and C. Düber are with the Department of Radiology, Johannes Gutenberg-University of Mainz, 55101 Mainz, Germany.

H.-U. Kauczor is with the Department of Radiology, German Cancer Research Center, Im Neuenheimer Feld 280, 69120 Heidelberg, Germany.

C. P. Heussel is with the Department of Radiology, Chest Clinic at University of Heidelberg, Amalienstrasse 5, 69126 Heidelberg, Germany.

Digital Object Identifier 10.1109/TMI.2007.902798

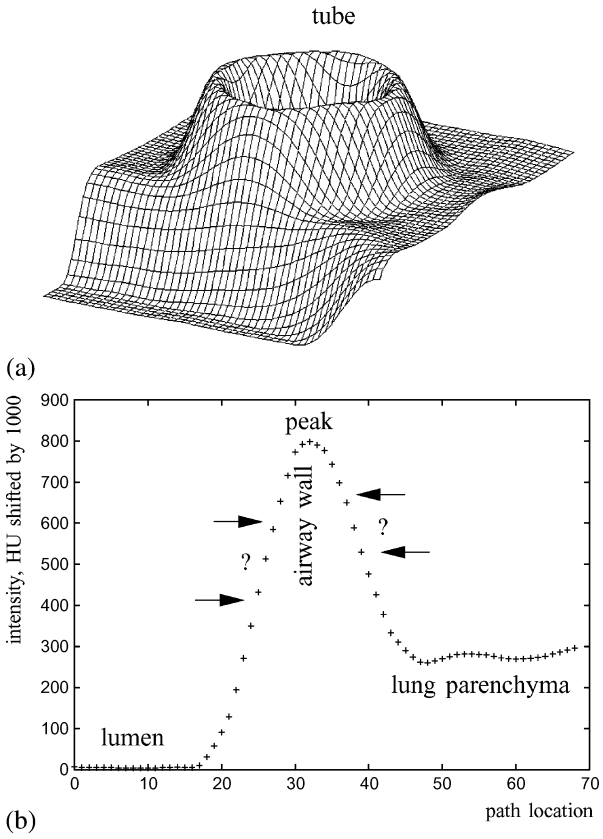

Fig. 1. (a) Representation of the X-ray density of a silicon tube with sharp edges on a single CT slice as topographical relief. This tube was surrounded by two different materials. The edges are blurred by the imaging system. (b) Cut through the relief (density profile) of a real bronchus wall of a pig. The arrows symbolize the dilemma: *Where is the exact boundary of the airway wall?*.

tween 2 and 4 mm. Subsequently the results achieved with the new method in real clinical CT volumes will be presented and discussed.

II. Theory

The inaccuracy of measuring thin structures like the airway walls in computed tomography has been noted by several authors [1], [11], [12]. Fig. 1 shows the difficulties in airway wall thickness measuring.

Dougherty and Newman clarified in a simulation and an experimental study [11], [12] the factors controlling image blurring in CT systems. The main effects causing an overestimation of thin structures in CT images are the blurring due to geometric effects such as the size and shape of the focal spot, the distances determining object magnification, X-ray scattering, limitations in the detector response, and the blurring caused by the reconstruction kernel used in the process of image reconstruction from projections. Different authors characterize the imaging performance by an overall system's point spread function [1], [5], [12], [13]. In the following, we denote the overall system's point spread function as PSF. There is additionally a blurring in digital systems caused by the finite sampling and the finite voxel size. We treat PSF and sampling separately. The blurring of an imaging system causes small objects in an image to be represented wider and less bright. The modulation transfer

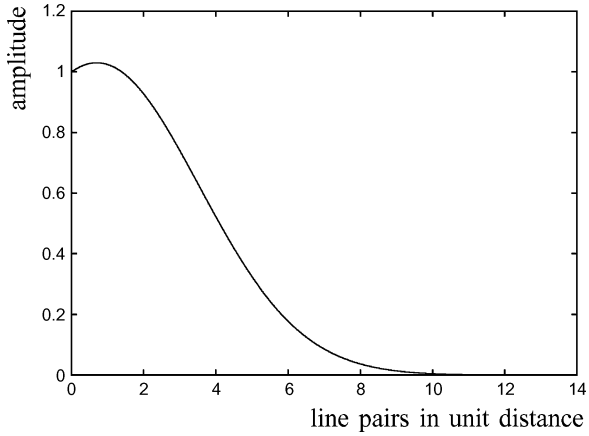

Fig. 2. Example of a modulation transfer function. The MTF documents the loss of amplitude for higher frequencies resp. more line pairs per unit distance (e.g., in [14, Ch. 25]). Hence, MTF documents the CT peak number loss for thin objects.

function (MTF) is a resolution measure describing this effect. It is the magnitude of the Fourier transformed PSF of the imaging system. The MTF curve describes how higher spatial frequencies are reduced in amplitude (see Fig. 2). In this way, contrast and resolution are combined in one standard measure. Most of the scanner's MTF curves results for low frequencies in amplitude values higher than 1.0, causing for example the well-known ringing effect in profiles of larger objects. Fig. 3 sums up the main problems causing the dilemma in measuring airway wall thickness.

Continuous 1-D, 2-D, or 3-D signals can be represented as functions

$$f_c(x), f_c(x,y), f_c(x,y,z). \tag{1}$$

Hence, a single 2-D image of a perfect continuous CT scanner, which gives an image of the reality coded in Hounsfield units (HU), can be written as $f_c(x,y)$. The sampled output of a perfect continuous CT scanner can now be defined as

$$f_s(x,y) = f_c(x,y)\mathrm{comb}(x,y,\Delta x,\Delta y) \tag{2}$$

with spacing $\Delta x, \Delta y$, where $\Delta x = \Delta y = \Delta x, y$ is the normal case.

An image of an real CT system can now be modeled as

$$\begin{aligned} f(x,y) &= \int_{-\infty}^{\infty}\int f_s(\xi,\upsilon)\mathrm{psf}_s(x-\xi,y-\upsilon)\mathrm{d}\xi\mathrm{d}\upsilon \\ &= f_s(x,y) * \mathrm{psf}_s(x,y). \end{aligned} \tag{3}$$

The model introduced in (3) can be used to represent 1-D, 2-D, and 3–D discrete signals generated from a CT system as $f(x)$, $f(x,y)$, and $f(x,y,z)$.

Thickness estimates with the FWHM method will only be accurate for standard convolution kernels when the true thickness is greater than 1.5–2.0 times the FWHM of the system's PSF, where the factor depends mainly on the convolution kernel [12]. Dougherty and Newman documented a linear relationship between the true thickness of a thin structure divided by the system's FWHM and the CT peak number of a profile across

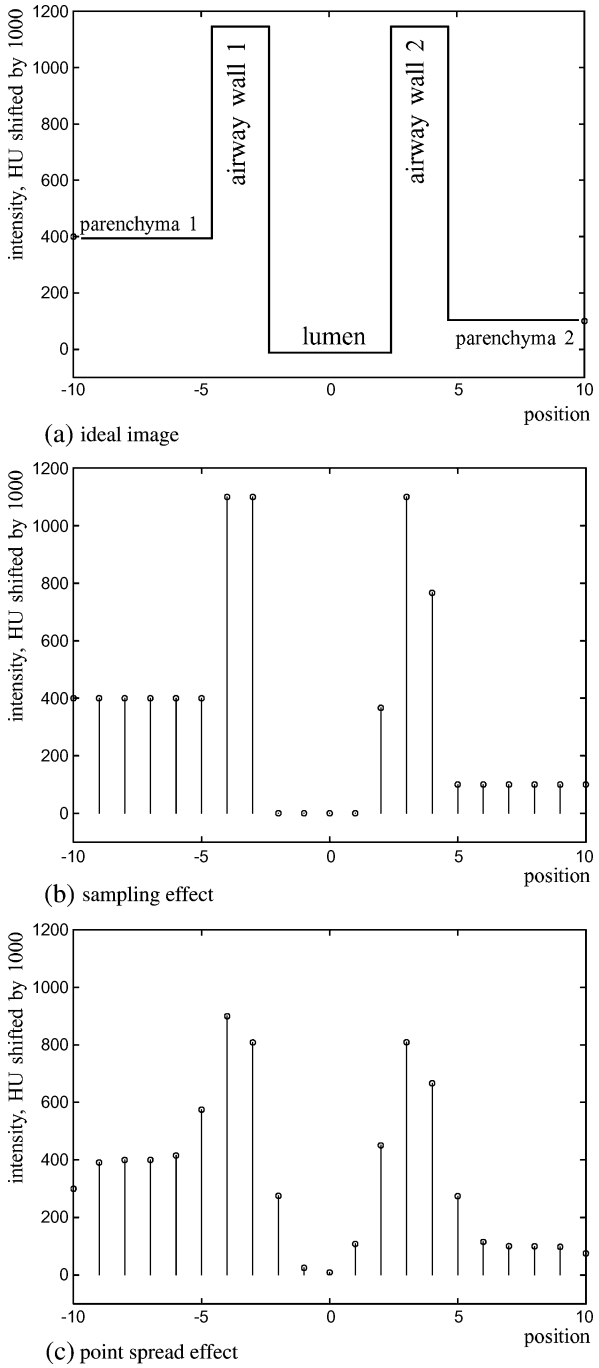

Fig. 3. (a) Intensity profile of an "ideal" airway expected by a "perfect" imaging system. (b) and (c) The ideal image above is blurred by the sampling effect and the system's overall PSF. This causes reduced intensity peaks and blurred edges. (b) Shows the sampling effect and (c) shows the result after blurring by the system's PSF. Note here, that the "same" walls in (a) result in different CT peak values in (c).

the structure [12]. The linear relationship is only true, if we are measuring thin structures with the same physical density, because the attenuation depends mainly on this parameter. Thus, for an exact measurement knowledge of either physical airway wall density or of the expected Hounsfield value is necessary in advance.[1]

[1]Another parameter influencing CT number is the atomic number of the material. We neglect the atomic number in the following.

If the measured CT peak number across a profile is below the expected CT value for the material, the thickness measured with FWHM would be an overestimation of the true thickness, therefore measuring at a higher percentage level on the profile could solve this problem. We denote the variable percentage level on a profile where the exact material thickness can be measured as best percentage level (BPL). Note that the same thin objects [e.g., airway wall 1 and airway wall 2 in Fig. 3(a)] can produce different profiles [see Fig. 3(c)] depending on the sampling of the CT system and the surrounding material, which is biasing the profiles as a consequence of convolution. So the system's PSF influences the BPL values and they are not stable for one specific material with a known thickness because of the sampling. A small field-of-view (FOV) should be used to minimize the effect of sampling and finite voxel size.

As mentioned before, the imaging performance of a CT system can be characterized by an overall 3-D point spread function. That is the fundamental characteristic of any linear imaging system. We additionally assume that CT systems are shift invariant. The PSF is an excellent basis for the analysis, design and enhancement of imaging systems. The PSF of spiral CT systems has hardly been studied and is rarely mentioned in literature. Often it was concluded that the PSF can be approximated by a 3-D Gaussian [15]. Schwarzband and Kiryati showed that the PSF of spiral CT has a complicated 3-D shape [16].

Even if we do not know the exact PSF of the system we assume that the integral of the system's integrated PSF fulfills the following, desirable equation in all directions:

$$\int_{-\infty}^{\infty} \mathrm{psf}(t)dt = 1. \tag{4}$$

For example, all normalized 3-D-Gaussians fulfill the (4) because they are symmetric and separable. If the system's PSF fulfills (4), the integral of a density profile along a certain infinite path in an infinite ideal image is equal to the integral of a density profile along the same path in the convolved image, because convolution does not change the integral. This is called the volume conservation property of convolution [13].

Unfortunately, the CT images and their density profiles are of finite size. If we want to use the conservation property of convolution, where shall the profiles through the airway walls start or end? Beside the system's PSF and the MTF curve the 10%–90% edge response is a well known parameter of the systems's resolution [14]. We decided therefore to use 10% level of the rising edge and the 10% level of the trailing edge as start and end point of the integral paths [Fig. 4(b)]. There are at least two advantages using 10% levels as start and end points. First, the locations are easy to find and secondly the whole wall is guaranteed to be imaged in the profile.

We can describe the problem of airway wall thickness measurement by the following linear system of equations:

$$a \cdot 0 + b \cdot \beta + c \cdot \alpha = \int_{\mathrm{edge}^1_{10\%}}^{\mathrm{edge}^2_{10\%}} f(t)dt \tag{5}$$

$$a + b + c = \left|\mathrm{edge}^1_{10\%}, \mathrm{edge}^2_{10\%}\right| \tag{6}$$

$$a - c = 0. \tag{7}$$

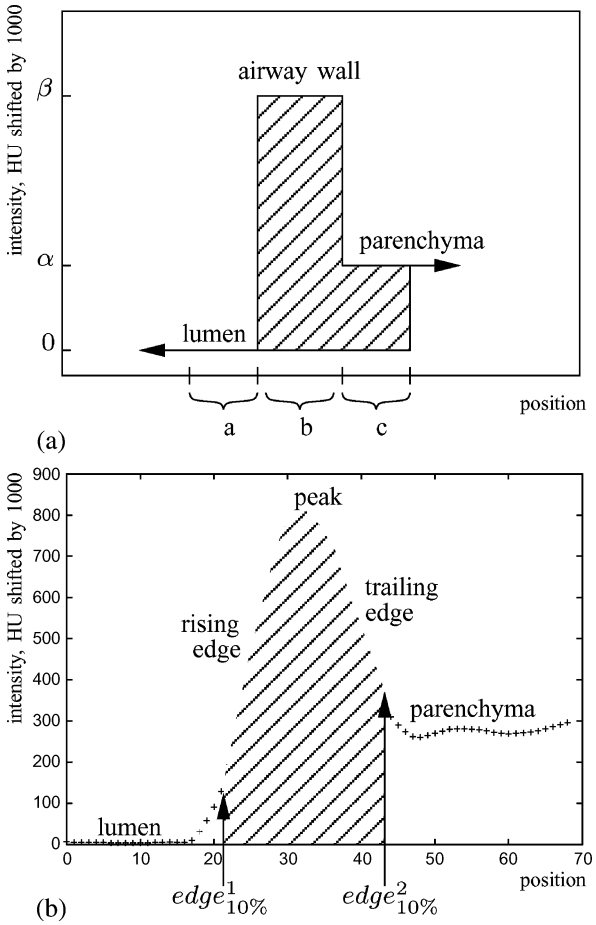

Fig. 4. (a) The diagram shows an intensity profile across an ideal 1-D airway model. a denotes the path length within the airway lumen, b denotes the path length within the airway wall and c denotes the path length within the surrounding lung parenchyma. The intensity of airway lumen is 0, the intensity of the airway wall is β and the intensity of the lung parenchyma is α. (b) Profile across an airway wall in a real CT image. The edges of the airway wall are blurred by the imaging system. $\mathrm{edge}^1_{10\%}$ denotes the 10% level of the rising edge and $\mathrm{edge}^2_{10\%}$ denotes the 10% level of the trailing edge.

The left-hand side of (5) represents the value of the integral in the airway model pictured in Fig. 4(a). a denotes the length of the path within the airway lumen, b denotes the path length in the airway wall and c denotes the path length within the surrounding lung parenchyma. The intensity of the airway lumen is 0 (shifted HU) whereas β represents the intensity of the airway wall and α represents the intensity of the lung parenchyma. The right-hand side is the value of the measured integral in the actual CT image, where $\mathrm{edge}^1_{10\%}$ denotes the 10% level of the rising edge and $\mathrm{edge}^2_{10\%}$ denotes the 10% level of the trailing edge pictured in Fig. 4(b). Equation (6) postulates that the path length of both integrals in (5) has to be equal. Equation (7) postulates that the edge response is equal on both sides of the profiles.

Solving the linear system (5)–(7) leads to following closed-form solution for an approximation of the airway's wall thickness:

$$b = \frac{\int_{\mathrm{edge}^2_{10\%}}^{\mathrm{edge}^1_{10\%}} f(t)dt - \frac{\alpha}{2}\left|\mathrm{edge}^2_{10\%}, \mathrm{edge}^1_{10\%}\right|}{\beta - \frac{\alpha}{2}}. \tag{8}$$

By using finite instead of infinite integration paths we lose information. Using a hard (sharp) reconstruction kernel leads to increased integral values. So we introduced a correction factor λ in (5), where λ depends on the system's PSF. Harder reconstruction kernels need smaller λ-values, because the finite integral is increased, softer kernels which produce Gaussian like PSFs need values >1, because the finite integral is decreased. In general, the correction factor λ depends additionally on the length of the integration path and is not a constant value. Measuring wider profiles requires λ-values near 1, Fig. 5(e) and (f) shows the dependency of λ on wall width. So (5) becomes

$$a \cdot 0 + b \cdot \beta + c \cdot \alpha = \lambda \int_{\mathrm{edge}^1_{10\%}}^{\mathrm{edge}^2_{10\%}} f(t)dt \tag{9}$$

and for the approximated wall thickness we arrive at

$$b = \frac{\lambda \int_{\mathrm{edge}^2_{10\%}}^{\mathrm{edge}^1_{10\%}} f(t)dt - \frac{\alpha}{2}\left|\mathrm{edge}^2_{10\%}, \mathrm{edge}^1_{10\%}\right|}{\beta - \frac{\alpha}{2}} \tag{10}$$

We validated the correctness of formula (10) with a 1-D convolution machine. We varied the main profile determining factors: the position of the wall in the discrete sampling grid, the wall thickness, the system's PSF and the value of the surrounding parenchyma. Fig. 5 gives an overview of the different tested situations. In all tested situations, the absolute error in the approximated wall thicknesses was very small, which is not surprising for this very artificial testing situation. We will document results with this new method more precisely for real CT volumes in Section IV.

III. Implementation of 3-D Method

A. Preliminary Algorithms: Segmentation, Skeletonization and Graph Representation

In a first step the lumen of the bronchial trees (respective of the tubes) is segmented as whole or in a 3-D box of interest with an automatic method introduced in [17]. The algorithm is based on a region growing process and determines if a voxel is air and if it is surrounded by airway wall. The growing conditions are selected very restrictively to prevent leaking out in the lung parenchyma. The voxel-based result (object) of the segmentation is skeletonized by a sequential topology-preserving 3-D thinning algorithm. The skeletonization is modeled after [18], [19]. North-, south-, east-, west-, top-, and bottom-border points are collected and deleted in iteration steps if they are simple, whereby a point is called "simple" point if its deletion does not alter the topology of the object. In this way, elongated objects are shrunk uniformly in each direction. The thinning process is completed when no further points could be deleted in an iteration step. In a next step, short terminal branches are eliminated by truncation and possible cycles are eliminated. Next, the skeleton is transformed to an acyclic graph similar to [20], whereby the branchings of the bronchi correspond to the nodes of the graph. Now it is possible to extract orthogonal planes to the skeleton paths between two branchings. After these preparatory steps, the bronchi or tubes can be measured within the computable orthogonal planes with the method described hereafter.

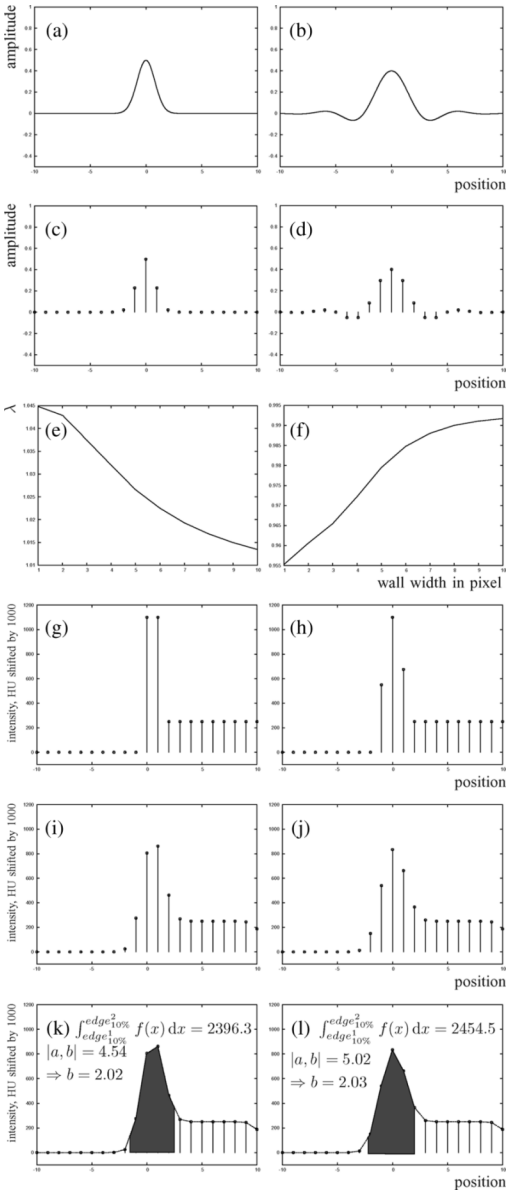

Fig. 5. Testing phase: beside the Gaussian displayed in (a) the windowed sinc function displayed in (b) was used as system's PSF. (c) and (d) Shows the discrete versions of the (a) and (b). (e) Shows the necessary λ-values for the calculation of the true wall thickness with formula (10) and $\alpha = 0$ for the Gaussian PSF and (f) for the sinc-based PSF. (g) The profile through an ideal airway-wall with width of exactly $2\Delta x$, where the wall fits perfectly into the sampling grid. (h) is a profile through an airway-wall with width of $2\Delta x$, where the wall does **not** fit perfectly into the sampling grid. (i) is the convolved signal of (g) with Gaussian PSF. (j) is the convolved signal of (h) with Gaussian PSF. (k) and (l) documents the results of formula (10) with correction factor $\lambda = 1.043$. $\lambda > 0$, because we used a the Gaussian in this example. If we set $\lambda = 1.05$ we get $b = 2.04$ and with $\lambda = 1.01$ we get $b = 1.94$ [in example (k)].

B. Wall Thickness Measurement

Let f be the discrete CT volume modeled after (3). Then $f : D_f \subset \mathbf{Z}^3 \rightarrow W_f \subset \mathbf{Z} \cap [-1024, 3071]$, because CT image data of up to date CT scanners is stored normally in 12 bit $(2^{12} = 4096)$ and ranges from -1024 to 3071 HU. f' denotes the extension of f to $\mathbf{R}^3$ by trilinear interpolation. $N = 128$ virtual rays are casted out from the center c of the airways orthogonal to the direction of the airways. c is defined by the skeletonization, the airway's orientation is given by the skeleton path

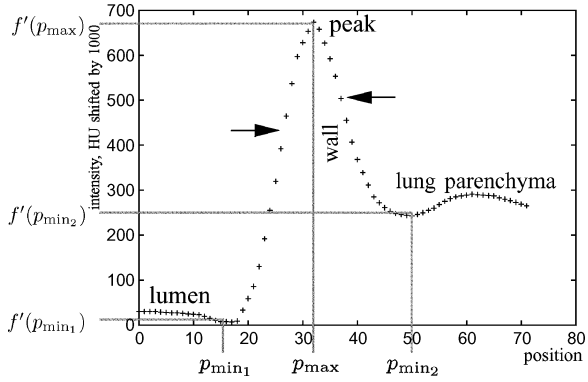

Fig. 6. The two arrows point to the calculated boundary points p_{wall_i} and p_{wall_o} of the airway wall.

between the two corresponding branchings. If the voxel-level skeleton points are to be used directly to determine the orientation of the airways, then the orientation can be off from the true direction. We calculate one direction vector from the two branch points and a second one from the direct skeleton neighbors of c. The average direction vector is used as airway direction. Profiles are generated from these virtual rays. A single profile is denoted as $l^i = \{p_0^i, p_1^i, \ldots, p_n^i\}$ where $i \in \{1, \ldots, N\}$. The profiles are calculated in the subvoxel domain and the endpoints of all profiles describe a whole circle around c. Then $p_k^i \in \mathbf{R}^3$, and we set the distance between two points p_k^i and p_{k+1}^i equal to the in-plane spacing $\Delta x, y$ of a single CT image (resampling). We used a ray length of 20 mm. $p^i_{\min_1}, p^i_{\max}$, and $p^i_{\min_2}$ are the points where f' assumes the first minimum in the lumen, the maximum in the wall and the next density minimum or plateau behind the wall (Fig. 6). Only profiles with a contrast higher than a predefined threshold between these values are processed (100 HU between lumen and wall, 20 HU between wall and parenchyma). Then the closed-form solution (10) can be used to approximate the wall thickness. Additionally, the inner and outer wall location, $p^i_{\text{wall}_i}$ and $p^i_{\text{wall}_o}$, can be calculated. We use $f'(p^i_{\min_2})$ as an approximation of α.

The N measurement results are sorted by the length of the integration path $|\text{edge}^2_{10\%}, \text{edge}^1_{10\%}|$. Short integration paths means sharp edges between two different materials. The final measurement result is defined as average value of the 25% shortest integration path results. We use two methods for the calculation of lumen and wall area, A_{lumen} and A_{wall}, in one plane. Assuming that the cross section of an ideal airway is nearly circular in shape the circle formula is used. The mean values for inner wall radius and outer wall radius are used as input variables. As a second method, an ellipse is fitted through the set of the airway edge points. The direct ellipse fitting method introduced by Fitzgibbon [21] is applied (see Appendix I).

In order to discriminate between "reliable" and "unreliable" measurements (e.g., in case of adjacent vessels) we adhere to the following error variables.

- The variance over all thickness measurements in one plane should be smaller than a threshold value. This accounts for the similarity of the N thickness measurements in one plane.

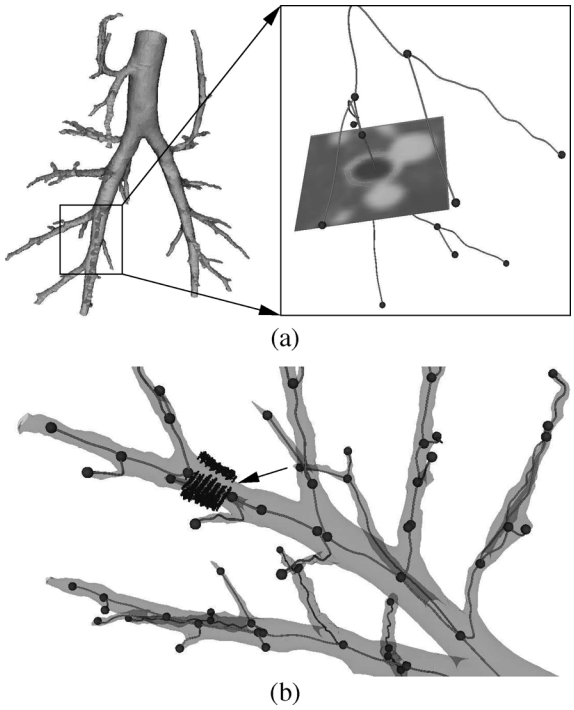

Fig. 7. (a) 3-D measurement of a pig bronchus in a box of interest. (b) One bronchus of a pig is measured. The dark points around the measured bronchus are the displayed CT peak values. The gap between the peak values (arrow) is caused by an adjacent blood vessel, where the algorithm can not find the peak values.

- More than $N/2$ of the profiles must be measurable in one plane.
- $|||p^i_{\text{wall}_i} - p^i_{\max}|| - ||p^i_{\text{wall}_o} - p_{\max}||| \leq 2\Delta x, y$ must be valid on a profile l^i. Note that a small difference between the inner wall thickness $||p^i_{\text{wall}_i} - p^i_{\max}||$ and the outer wall thickness $||p^i_{\text{wall}_o} - p^i_{\max}||$ is normal because of the discrete sampling.
- $|(A^{\text{circle}}_{\text{lumen}}/A^{\text{ellipse}}_{\text{lumen}}) - 1|$ should be smaller than a threshold value. This should confirm the calculated direction vector.

Additionally the first two and the last two skeleton points on an edge are *a priori* not used for the measurement, because these measurements are always influenced by the branching points.

C. Global 3-D Tree Analysis

The method is not limited to the analysis of airways sliced orthogonal by the original scanning plane. It is possible to measure all bronchi segmented with the used segmentation method (see e.g., Fig. 7). Thus, a global analysis of the segmented bronchial tree can be done.

We define

$$\text{wall}\% := A_{\text{wall}}/A_{\text{total}} \cdot 100 \tag{11}$$

where A_{wall} denotes the wall area and $A_{\text{total}} = A_{\text{lumen}} + A_{\text{wall}}$ denotes the total airway area. Measurement of just a few bronchi in a dataset can be misleading, because a possible disease is not necessarily distributed homogeneously. To circumvent this we defined a global bronchial tree value as

$$\text{GBT}_{3,8} := \underset{3 \leq d_0 \leq 8}{\text{mean}} \text{wall}\%. \tag{12}$$

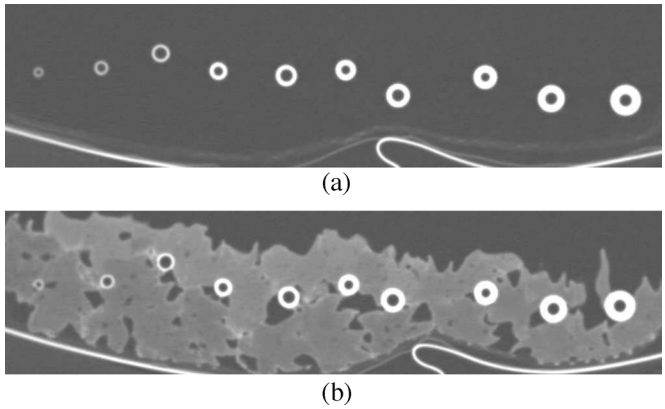

Fig. 8. (a) The phantom containing 10 tubes orthogonal to the scanning plane. (b) Phantom orthogonal to scanning plane surrounded by spray cream, modeling lung parenchyma.

We used the interval [3,8] because the outer diameters d_o from most of the segmented bronchi are in this range. The wall thickness for the first several generations of the healthy human airway tree is approximately 10%–16% of the inside diameter [22]. With the inner radius of an airway denoted as r_i and the outer as r_o, wall thickness w can be written as $w = r_o - r_i$ and

$$w/2r_i = q \quad \text{with} \quad q \in [0.1, 0.16]. \tag{13}$$

So we get a linear relationship between wall thickness w and inner radius r_i. Hence, we get

$$\text{wall}\% = \frac{\pi\left(r_o^2 - r_i^2\right)}{\pi r_o^2} \cdot 100 = \left(1 - \left(\frac{1}{1+2q}\right)^2\right) \cdot 100 \tag{14}$$

wall% for the first several generations in the range of 31%–43% for a healthy human. In reality, we can not really expect a precise constant because the airway wall is not a homogeneous material and the consistency is varying along the bronchial tree [23], [24], especially in diseased lungs.

IV. Results

A. Phantom Measurements

In order to prove the closed-form solution in real CT images we performed several phantom measurement series.

We scanned a phantom containing 10 tubes (silicone tubes, Deutsch&Neuman GmbH, Berlin, Germany, range of wall thicknesses: 0.3–2.5 mm, range of outer diameters: 2.6–9.0 mm) with a Philips Multislice-CT scanner (Brilliance CT 64, Philips Medical Systems, The Netherlands), see Fig. 8. Table I lists the geometry of the tubes. Wall thickness is monotonically increasing from tube no. 1 to no. 10. Reconstructions were done with B and the harder L kernel as well as a voxel size of $0.19 \times 0.19 \times 0.9\ \text{mm}^3$ (FOV 1) and $0.35 \times 0.35 \times 0.9\ \text{mm}^3$ (FOV 2) with slice increment 0.45 mm. All tubes had the same physical density $\rho = 1,14\ \text{g/cm}^3$. The CT peak values obtained from the 10 tubes for the two FOVs and both reconstructions kernels are tabulated in Table I. Because of the correlation between CT numbers and the density ρ, an expected CT number can be calculated with the conversion method introduced in [25]. We obtained a CT number of ≈207 HU, based on specific

TABLE I
GEOMETRY OF THE 10 TUBES

$no.$	1	2	3	4	5
w	0.3	0.4	0.5	1.0	1.0
d_i	2.0	3.0	4.0	3.0	4.0
d_o	2.6	3.8	5.0	5.0	6.0
p_1	-663	-514	-360	39	137
p_2	-749	-652	-542	-200	-148
p_3	-665	-538	-388	8	93
p_4	-747	-659	-551	-214	-155
$wall\%$	41	38	36	64	56

$no.$	6	7	8	9	10
w	1.5	1.5	2.0	2.0	2.5
d_i	3.0	4.0	3.0	4.0	4.0
d_o	6.0	7.0	7.0	8.0	9.0
p_1	280	282	345	315	366
p_2	44	44	184	157	245
p_3	252	257	337	308	361
p_4	33	30	172	143	230
$wall\%$	75	67	82	75	80

Abbreviations used in this and the following tables: Number of tube (*no.*), wall thickness (w), inner diameter (d_i), outer diameter (d_o), measured wall thickness ($\bar{w}$), absolute error Δw and relative error $\%w$. CT peak value for FOV 1 kernel L (p_1), FOV 1 kernel B (p_2), FOV 2 kernel L (p_3) and FOV 2 kernel B (p_4). CT peak values higher than the expected CT number $\approx$207 HU are caused by the amplitude values higher than 1.0 in the scanner's MTF curve.

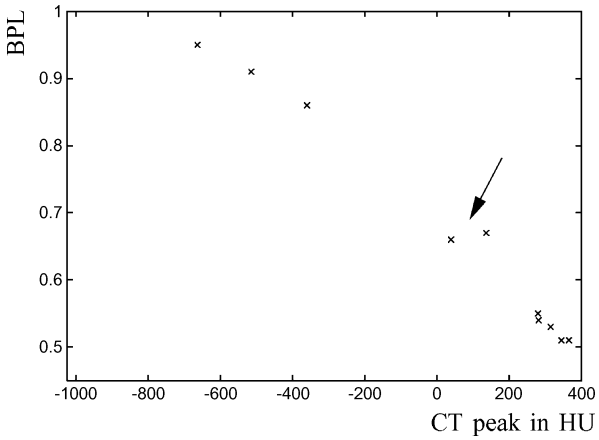

Fig. 9. Necessary BPL values in order to get the true wall thickness of the 10 artificial tubes. Reconstruction of the underlying images was done with the L kernel and FOV 1. Tubes with smaller walls generate smaller CT peak values. There are slightly higher CT peak values for wider walls than the expected CT number of $\approx$207 HU. This effect is caused by amplitude values higher than 1.0 in the scanner's MTF curve (see Section II). The arrow points to tubes no. 4 and no. 5 with the same wall thickness but significant different CT peak numbers (39 HU and 137 HU). This is mainly caused by the different diameter of the two tubes, biasing the CT peak number via convolution. Obviously, there is no bijective map between BPL values and CT peak values. Note, that it is also possible to have different wall thicknesses with equal CT peak values—that is caused by the shape of the scanner's MTF curve—it is not an invertible function (see Fig. 2). In general there is no exact linear relationship between BPL values and CT peak values.

density. Fig. 9 shows the required BPL values for an accurate measurement for these tubes. In a second series, the tubes were

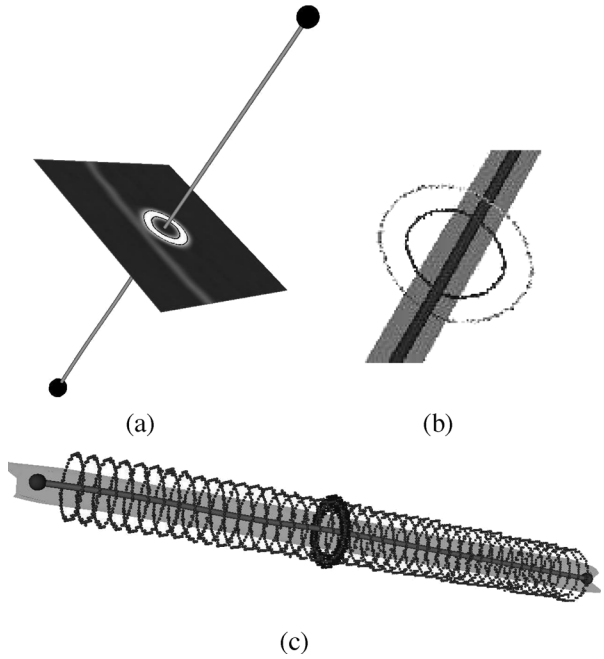

Fig. 10. (a) The graph of a tube contains exactly one edge and two endpoints. An orthogonal plane to the direction of the edge is displayed. (b) Calculated inner and outer wall of a tube. (c) Many measurements can be done at one tube.

TABLE II
PHANTOM MEASUREMENT—TABLE COMPARES THE RESULTS ACHIEVED WITH THE FWHM METHOD FOR B KERNEL AND L KERNEL (FOV 1, 90° SCAN)

	FOV 1 Kernel B & 90°			FOV 1 Kernel L & 90°		
$no.$	$\tilde{w}$	Δw	$\%w$	$\tilde{w}$	Δw	$\%w$
1	1.20	0.90	299.67	1.25	0.95	318.00
2	1.57	1.17	292.00	1.13	0.73	183.00
3	1.50	1.00	200.00	1.10	0.60	120.00
4	1.65	0.65	64.70	1.29	0.29	28.80
5	1.64	0.64	64.00	1.30	0.30	30.30
6	1.86	0.36	23.87	1.59	0.09	5.73
7	1.84	0.34	22.67	1.58	0.08	5.53
8	2.22	0.22	10.75	2.02	0.02	0.90
9	2.24	0.24	12.10	2.06	0.06	3.00
10	2.65	0.15	6.00	2.52	0.02	0.84

scanned surrounded by spray cream, with a mean CT density of ≈ -750 HU, simulating the lung parenchyma. We scanned the tubes orthogonal to the scanning plane and additionally in an angle of 45° to the scanning plane. We adjusted the λ factor to the two different kernels by measuring tube no. 10 (FOV 1, 90° scan). We used $\lambda = 0.90$ (constant for all tubes) for the scans reconstructed with kernel L and $\lambda = 0.93$ for the scans reconstructed with kernel B. Most measurement results are tabulated in the following.

Fig. 10 shows explanatory screenshots of the measurement procedure. The calculated inner and outer radii depend mainly on the calculated wall thickness, so the result tables contains just the wall thickness results.

Table II documents the results achieved with the simple FWHM method. The mean absolute error (relative error) for the wall thickness in Table II was 0.31 mm (70%) for the L

TABLE III
PHANTOM MEASUREMENT—COMPARISION OF THE RESULTS ACHIEVED WITH THE INTEGRAL BASED METHOD FOR FOV 1 AND FOV 2 (KERNEL B, 90° SCAN)

	FOV 1 Kernel B & 90°			FOV 2 Kernel B & 90°		
no.	$\tilde{w}$	Δw	$\%w$	$\tilde{w}$	Δw	$\%w$
1	0.29	-0.01	2.67	0.31	0.01	3.67
2	0.41	0.01	2.00	0.42	0.02	4.25
3	0.54	0.04	7.60	0.54	0.04	7.80
4	1.03	0.03	2.50	1.03	0.03	3.00
5	1.02	0.02	2.40	1.06	0.06	5.80
6	1.48	-0.02	1.20	1.49	-0.01	0.87
7	1.50	0.00	0.27	1.49	-0.01	0.53
8	2.02	0.02	0.90	2.02	0.02	0.80
9	1.98	-0.02	1.15	1.99	-0.01	0.50
10	2.50	0.00	0.12	2.51	0.01	0.40

TABLE IV
PHANTOM MEASUREMENT—COMPARISION OF THE RESULTS ACHIEVED WITH THE INTEGRAL BASED METHOD FOR SCAN ANGLES OF 45° AND 90° (KERNEL L, FOV 1)

	FOV 1 Kernel L & 90°			FOV 1 Kernel L & 45°		
no.	$\tilde{w}$	Δw	$\%w$	$\tilde{w}$	Δw	$\%w$
1	0.29	-0.01	2.33	0.31	0.01	1.67
2	0.41	0.01	3.50	0.43	0.03	6.75
3	0.54	0.04	7.60	0.53	0.03	5.80
4	1.01	0.01	0.60	1.01	0.01	1.40
5	1.03	0.03	3.30	1.04	0.04	4.10
6	1.49	-0.01	0.67	1.48	-0.02	1.07
7	1.50	0.00	0.33	1.49	-0.01	0.60
8	1.99	-0.01	0.30	1.98	-0.02	1.20
9	1.98	-0.02	0.80	1.97	-0.03	1.35
10	2.50	0.00	0.16	2.52	0.02	0.92

kernel and FOV 1. The maximal relative error occured for the smallest tube (no. 1) with 318%. Note that even the monotonic increasing wall thickness from tube no. 1 to no. 10 is not conserved by the FWHM method. For the B kernel and FOV 1 the mean errors were 0.57 mm (100%). The mean errors with FWHM were larger for FOV 2.[2] 0.36 mm (77%) for kernel L and 0.60 mm (104%) for kernel B.

The following tables documents the results achieved with the new integral based method. The mean errors in Table III were for FOV 1 0.02 mm (2%) and for FOV 2 0.02 mm (3%). These were the results for the B kernel and 90° scan. For the L kernel we achieved for FOV 1 0.01 mm (2%) and for FOV 2 0.02 mm (2%).[2] Mean errors were slightly larger for FOV 2.

In Table IV the mean errors were 0.01 mm (2%) for the 90° scan, reconstructed with kernel L and FOV 1, and 0.02 mm (2%) for the 45° scan. For FOV 2 the mean errors were 0.02 mm (2%) for the 90° scan and 0.03 mm (4%) for the 45° angle scan.[2] So small differences between the results for different angles were observed.

[2]single results not tabulated.

TABLE V
PHANTOM MEASUREMENT—COMPARISION OF THE RESULTS ACHIEVED WITH THE INTEGRAL BASED METHOD FOR SCAN ANGLES OF 45° AND 90° (SPRAY CREAM, KERNEL L, FOV 1)

	FOV 1 & Kernel L & Spray Cream & 90°			FOV 1 & Kernel L & Spray Cream & 45°		
no.	$\tilde{w}$	Δw	$\%w$	$\tilde{w}$	Δw	$\%w$
1	0.31	0.01	2.33	0.33	0.03	9.67
2	0.41	0.01	3.00	0.44	0.04	8.75
3	0.53	0.03	6.40	0.55	0.05	9.60
4	0.98	-0.02	1.70	1.03	0.03	3.30
5	1.03	0.03	2.60	1.06	0.06	6.00
6	1.48	-0.02	1.53	1.47	-0.03	2.13
7	1.47	-0.03	1.87	1.50	0.00	0.07
8	1.95	-0.05	2.55	1.98	-0.02	1.00
9	1.94	-0.06	2.85	1.95	-0.05	2.40
10	2.47	-0.03	1.40	2.50	0.00	0.12

TABLE VI
PHANTOM MEASUREMENT—COMPARISION OF THE RESULTS ACHIEVED WITH THE INTEGRAL BASED METHOD FOR SCAN ANGLES OF 45° AND 90° (SPRAY CREAM, KERNEL L, FOV 2)

	FOV 2 & Kernel L & Spray Cream & 90°			FOV 2 & Kernel L & Spray Cream & 45°		
no.	$\tilde{w}$	Δw	$\%w$	$\tilde{w}$	Δw	$\%w$
1	0.36	0.06	19.33	0.35	0.05	18.00
2	0.42	0.02	4.25	0.36	-0.04	9.75
3	0.55	0.05	9.00	0.54	0.04	7.00
4	1.03	0.03	2.90	1.01	0.01	1.00
5	1.09	0.09	8.70	1.08	0.08	8.20
6	1.51	0.01	0.67	1.47	-0.03	1.87
7	1.51	0.01	0.80	1.50	0.00	0.20
8	1.96	-0.04	2.20	1.97	-0.03	1.55
9	1.96	-0.04	2.20	1.95	-0.05	2.65
10	2.47	-0.03	1.08	2.52	0.02	0.96

Tables V and VI shows the results of the most difficult testing situations, where the tubes were surrounded by the spray cream, modeling lung parenchyma. The mean errors for the 90° angle scan and FOV 1 were 0.03 mm (3%) and for the 45° angle scan 0.03 mm (4%). The errors were larger for FOV 2. 0.04 mm (5%) for the 90° scan and 0.04 (5%) for the 45° scan.

The new integral based method delivers in generally good results in all testing situations. The largest errors occur in the most difficult testing situations. The relative error is in generally slightly larger for the smaller walls.

B. Global 3-D Tree Analysis

Fig. 11 shows plots generated from global measurement results in a human dataset. Fig. 11(a) shows the wall% values plotted versus outer diameter. Note, that for a particular outer diameter an interval of wall% is measured.

Fig. 11(b) shows the CT peak values plotted versus outer diameter and Fig. 11(c) documents the linear relationship derived in (13). The linear relationship can clearly be seen for the bronchi smaller than 8 mm.

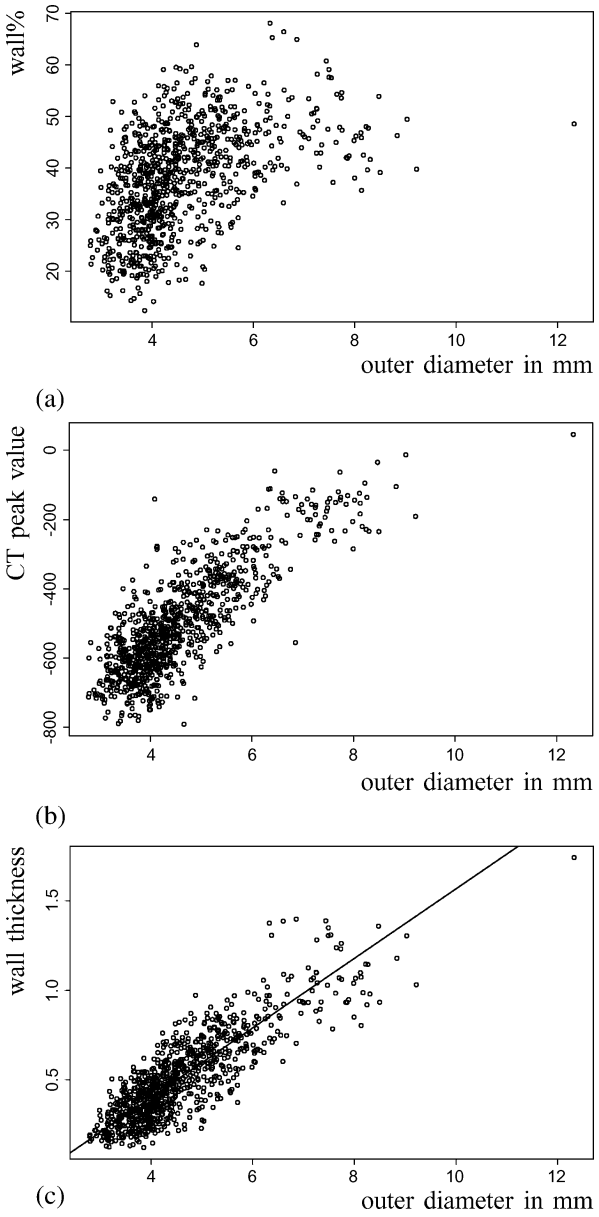

Fig. 11. (a) Wall% versus outer diameter. For a single outer diameter a range for wall% is measured. $\mathrm{GBT}_{3,8} = 38.10$. (b) CT peak value versus outer diameter. (c) Wall thickness calculated versus outer diameter. Parameters of the linear fit: $\mathrm{slope} = 0.194$, $R^2 = 0.702$, $\mathrm{residual\ standard\ error} = 0.128$. Plots (a)–(c) were generated from a human dataset. The software calculated the wall thickness in 904 orthogonal planes.

It should be clear, that even if we could do a perfect measurement of the airway geometry these values may differ between two scans of the same individual, because wall% depends also on the respiration state of the individual, since the area respective volume of lumen is not constant. Furthermore there might be a change of respiration state during scanning the individual. Therefore, the next section addresses the issue of repeatability.

C. Repeatability of Global 3-D Tree Analysis

In order to prove the repeatability of the measurements in real lungs, eight pigs were scanned twice with the same scanning protocol in a short time interval after repositioning on the CT scanner. The pigs were mechanically ventilated and the scans were acquired during an inspiratory breath hold. All datasets were reconstructed with the same kernel. The voxel size was $0.31 \times 0.31 \times 1.0\ \mathrm{mm}^3$. The maximal absolute error in the $\mathrm{GBT}_{3,8}$ values between two measurements was 1.22 and the mean error was 0.60 (see Fig. 12).

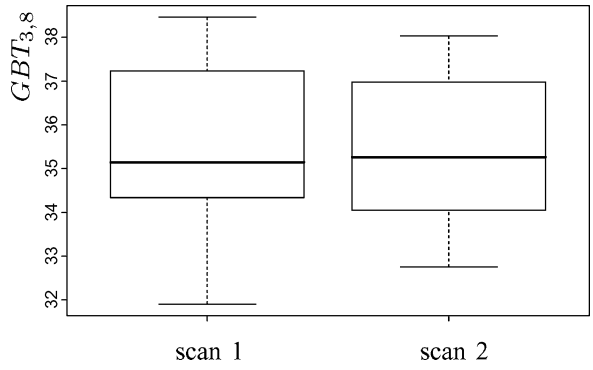

Fig. 12. Box-and-whisker diagrams of the $\mathrm{GBT}_{3,8}$ values in two different scans of the same eight pigs. The Pearson correlation coefficient of the $\mathrm{GBT}_{3,8}$ values between the two scans was $r = 0.93$. The median $\mathrm{GBT}_{3,8}$ for scan 1 was 35.14 and for scan 2 35.26.

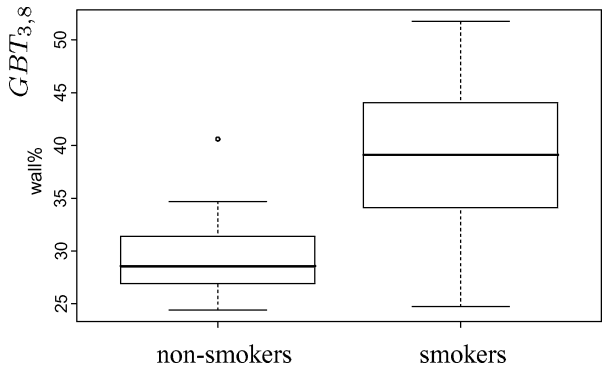

Fig. 13. Box-and-whisker diagrams of the 16 smokers (median $\mathrm{GBT}_{3,8}$ value 39.12) and 15 nonsmokers (median $\mathrm{GBT}_{3,8}$ value 28.56) datasets.

D. Global Analysis Results in Smoker and Nonsmoker Datasets

Is the global analysis method able to characterize a population of smokers and nonsmokers? We analyzed 16 smokers with a smoking history of 50 ± 25 pack-years (range 21–135 pack-years) and 15 nonsmoker CT datasets with no history of smoking. All datasets were acquired with the same CT scanner and reconstructed with the same reconstruction kernel. The voxel size was $0.39 \times 0.39 \times 1.0\ \mathrm{mm}^3$. The median $\mathrm{GBT}_{3,8}$ value for the smokers was 39.12 (mean 38.86, range 24.73–51.74) and for the nonsmokers 28.56 (mean 29.62, range 24.40–40.60). The median $\mathrm{GBT}_{3,8}$ values were significantly differenten for the two groups (two-sided Wilcoxon rank sum test: $p = 0.0008$, see Fig. 13). The median slope of the linear fit between the wall thickness and the outer airway diameter [see example plot Fig. 11(c)] was 0.18 (mean 0.18, range 0.11–0.29) for the smokers and 0.14 (mean 0.14, range 0.10–0.22) for the nonsmokers. The slope was significant higher for the smokers (two-sided Wilcoxon rank sum test: $p = 0.0041$).

So in this trial the new method was able to discriminate between the smokers and the nonsmokers. Further clinical trials with smokers and nonsmokers are ongoing.

The average runtime on a PC (Intel Pentium 4, 3.0 GHz, 2 GB RAM) for the preliminary algorithms (segmentation, skeletonization and graph representation) was 202 s (range 176–238 s). The average runtime for the global analysis of the smoker and nonsmoker airway trees was 406 s (range 296–501 s) and depends on the size of the tree and the image quality.[3] More than 500 "reliable" measurements per patient were written in a text file on the average.

Note that $\mathrm{GBT}_{3,8}$ is a global bronchial tree value and depends on the segmented bronchial tree. So $\mathrm{GBT}_{3,8}$ will be influenced if a disease is not distributed homogeneously or affected bronchi are not detected by the used segmentation algorithm. We used the segmentation results of the automatic method introduced in [17].

For statistical evaluation, GNU R 2.3.1 for Windows, was used.

V. Discussion

We addressed the problems in airway wall measuring respectively the problems in measuring thin structures in CT images. We showed the relationship between the physical density, amplitude and contrast in CT images and derived a closed-form solution to circumvent these problems. Our integral-based method requires a calibration step to adjust the λ factor to different scanning parameters. Another drawback of the method is that we need an expected Hounsfield value of the material we are measuring. Once the method is calibrated it works with any kind of material and needs no manual interaction. Of course the CT density is not constant for the whole bronchial tree, because it consists of different tissues (muscle layers, cartilage, calcified cartilage, mucus, etc.) and different compositions if these tissues. Differing CT densities can be expected. An optimization could be the dynamical adjustment of β in (10), which is a task for the future. We used $N = 128$ virtual rays for the measurement within an orthogonal plane. It is maybe possible to use less rays without losing precision in the measurement results. Additional sources of measurement bias may the selection of profiles with a contrast higher than a predefined threshold, the presorting of the measurement results by the length of the integration path and the used error variables to discriminate between "reliable" and "unreliable" measurements. We aimed to exclude questionable measurement locations by these maneuvers. Our new algorithm has to be calibrated to a scanner protocol by setting the correction factor λ depending on the PSF of the imaging system. We did not address the influence of the radiation exposure to the system's PSF—but an exposure-change as well as patient's body size influences the CT image and consequently the profiles through the airway walls. At least the radiation exposure was held constant in our patient studies. Additionally, as we mentioned before, λ is not a constant, it depends on the length of the integration path. We used constant λ values for all tube sizes in the phantom measurement series. The algorithm seems not to be very sensitive to the lambda values, the phantom measurement results with constant λ's were better than we expected. A possible explanation could be the not considered curvature of the walls (curved internal and external surface) or the possibly nonseparable PSF of the CT system. The method of Saba *et al.* [5] was validated using a plexiglas phantom containing five plexiglas tubes with wall thicknesses between 1.16 and 3.05 mm. Wall thicknesses of the bronchi inside of highest medical diagnostic interest are $\leq$1.0 mm as lung function is supposed to be partly determined by the small conducting airways [26]. So we do not know how well the method works inside this range. They wrote that the model-based method is able to estimate airway geometry to within one-half a 0.29-mm pixel (in general, with exceptions) for a standard reconstruction. The iterative method introduced in [7] showed good results for estimating the inner diameter of the used plexiglas phantom. They used three different scan settings (low dose, regular dose, high dose) with a voxel size of $0.39 \times 0.39 \times 0.6\ \mathrm{mm}^3$ and the average absolute deviation from the nominal diameter never exceeded 0.26 mm. Wall thickness measurements are not reported.

The results of our new method assessing airway phantoms obviously show that the assumptions (4) and (7) were a good choice. Measurements with the simple FWHM method results in unacceptable large errors for wall thicknesses smaller than $\leq$1.0 mm. We showed that our method works well with all tested tubes even with very small wall thicknesses of tubes no. 1–no. 3. All reported results for the wall thickness measurements in the phantom scans were smaller than 1/3 of the in-plane spacing. The results for the inner and outer radii (not tabulated in the results section) were smaller than 1/2 of the in-plane spacing.

The introduced $\mathrm{GBT}_{3,8}$ value shows good repeatability and is a single parameter describing the bronchial tree of a patient, based in general on hundreds of measurements. A parameter depending on the generation numbers of the bronchi is desirable, especially from a medical and medical–scientific point of view. However our automatic bronchial tree labeling is not reliable up to now. Tschirren *et al.* showed in [7] good results in bronchial tree labeling. An improved labeling is a further task for future improvements of our software.

Appendix I
Ellipse Fitting

The original ellipse fitting algorithm was introduced by Fitzgibbon [21] as a Matlab implementation. Here, is the slighty different GNU Octave script with some extensions.

Octave-Script

```
%build design matrix: vector a contains the coordinates
D = [a(:,1).*a(:,1), a(:,1).*a(:,2), a(:,2).*a(:,2), a(:,1), a(:,2), ones(rows(a),1)];
%build scatter matrix
S = D' * D;
%build constrain matrix
C(6,6) = 0; C(1,3) = 2; C(2,2) = -1; C(3,1) = 2;
[AA, BB, Q, Z, V, W, lambda] = qz(S, C);
```

[3]The most time consuming part is the ellipse fitting algorithm (see Appendix I), because it is implemented as a GNU Octave script and used via a pipe. We plan to rewrite this in pure C++.

$$[\max\_lambda, \max\_lambda\_index] = \max(lambda);$$

$$u\_i = V(:, \max\_lambda\_index)' * C*V(:, \max\_lambda\_index);$$

$$my = sqrt(1/u\_i);$$

$$a\_dach = my * V(:, \max\_lambda\_index);$$

% – extensions –

% transformation of ellipse to normal form

%see e. g. [27] chapter 2.6.6.2 Geometrie

$$A\_normal = [a\_dach(1), a\_dach(2)/2; a\_dach(2)/2, a\_dach(3)];$$

$$A\_schlange = [a\_dach(1), a\_dach(2)/2, a\_dach(4)/2; a\_dach(2)/2, a\_dach(3), a\_dach(5)/2; a\_dach(4)/2, a\_dach(5)/2, a\_dach(6)];$$

$$a\_strich = \det(A\_schlange)/\det(A\_normal);$$

$$lambda\_A\_normal = eig(A\_normal);$$

$$f\_a = sqrt(-a\_Strich/lambda\_A\_normal(1));$$

$$f\_b = sqrt(-a\_Strich/lambda\_A\_normal(2));$$

$$\%ellipse = (1/f\_a\^2) * x\^2 + (1/f\_b\^2) * y\^2 = 1$$

$$area = pi * f\_a * f\_b$$

% calculation of ellipse center

$$a\_normal = [-a\_dach(4)/2; -a\_dach(5)/2]$$

$$center = A\_Normal \setminus a\_normal$$

%determination of ellipse axis

%see e. g. [27] chapter 2.4.4.5.3 Geometrie

$$[EV, EW] = eig(A\_Normal)$$

% EV contains the normalized eigenvektors of matrix A_Normal

$$axis1 = f\_a * EV(:, 1)$$

$$axis2 = f\_b * EV(:, 2)$$

ACKNOWLEDGMENT

This paper is dedicated to the memory of Dr. T. Uthmann.

REFERENCES

[1] J. M. Reinhardt, N. D. D'Souza, and E. A. Hoffman, "Accurate measurement of intra-thoracic airways," *IEEE Trans. Med. Imag.*, vol. 16, no. 6, pp. 820–827, Dec. 1997.

[2] G. G. King, N. L. Müller, K. P. Whittall, Q. Xiang, and P. D. Pare, "An analysis algorithm for measuring airway lumen and wall areas from high-resolution computed tomographic data," *Am. J. Respiratory Crit. Care Med.*, vol. 161, no. 2, pp. 574–580, 2000.

[3] Y. Nakano, S. Muro, H. Sakai, T. Hirai, K. Chin, M. Tsukino, K. Nishimura, H. Itoh, P. D. Paré, J. C. Hogg, and M. Mishima, "Computed tomographic measurements of airway dimensions and emphysema in smokers," *Am. J. Respir. Crit. Care Med.*, vol. 162, no. 3, pp. 1102–1108, Sep. 2000.

[4] F. Chabat, X.-P. Hu, D. M. Hansell, and G.-Z. Yang, "ERS transform for the automated detection of bronchial abnormalities on CT of the lungs," *IEEE Trans. Med. Imag.*, vol. 20, no. 9, pp. 942–952, Sep. 2001.

[5] O. Saba, E. A. Hoffman, and J. M. Reinhardt, "Maximizing quantitative accuracy of lung airway lumen and wall measures obtained from X-ray CT imaging," *J. Appl. Physiol.*, vol. 95, pp. 1063–1095, 2003.

[6] M. Remy-Jardin, A. Amara, P. Campistron, I. Mastora, V. Delannoy, A. Duhamel, and J. Remy, "Diagnosis of bronchiectasis with multislice spiral CT: Accuracy of 3-mm-thick structured sections," *Eur. Radiol.*, vol. 13, pp. 1165–1171, 2003.

[7] J. Tschirren, E. A. Hoffman, and M. Sonka, "Intrathoracic airway trees: Segmentation and airway morphology analysis from low-dose ct scans," *IEEE Trans. Med. Imaging*, vol. 24, no. 12, pp. 1529–1539, Dec. 2005.

[8] E. Y. Kang, R. R. Miller, and N. L. Müller, "Bronchiectasis: Comparison of preoperative thin-section CT and pathologic findings in resected specimens," *Radiology*, vol. 195, pp. 649–654, 1995.

[9] D. A. Lynch, J. D. Newell, B. A. Tschomper, T. M. Cink, L. S. Newman, and R. Bethel, "Uncomplicated asthma in adults: Comparison of CT appearance of the lungs in asthmatic and healthy subjects," *Radiology*, vol. 188, pp. 829–833, 1993.

[10] B. L. Odry, A. P. Kiraly, C. L. Novak, D. P. Naidich, and J. F. Lerallut, "Automated airway evaluation system for multi-slice computed tomography using airway lumen diameter, airway wall thickness and broncho-arterial ratio," in *Proc. SPIE*, 2006, vol. 6143, pp. 243–253.

[11] D. Newman, G. Dougherty, A. A. Obaid, and H. A. Hajrasy, "Limitations of clinical CT in assessing cortical thickness and density," *Phys. Med. Biol.*, vol. 43, pp. 619–626, 1998.

[12] G. Dougherty and D. Newman, "Measurement of thickness and density of thin structures by computed tomography: A simulation study," *Med. Phys.*, vol. 26, no. 7, pp. 1341–1348, 1999.

[13] A. K. Jain, *Fundamentals of Digital Image Processing*. New York: Prentice-Hall, 1989.

[14] S. W. Smith, *The Scientist and Engineer's Guide to Digital Signal Processing*. San Diego, CA: California Technical Publishing, 1999.

[15] G. Wang, M. W. Vannier, M. W. Skinner, M. G. P. Cavalcanti, and G. W. Harding, "Spiral CT image deblurring for cochlear implantation," *IEEE Trans. Med. Imag.*, vol. 17, no. 2, pp. 251–262, Apr. 1998.

[16] G. Schwarzband and N. Kiryati, "The point spread function of spiral ct," *Phys. Med. Biol.*, vol. 50, pp. 5307–5322, 2005.

[17] O. Weinheimer, T. Achenbach, C. Buschsieweke, C. P. Heussel, T. Uthmann, and H.-U. Kauczor, "Quantification and characterization of pulmonary emphysema in multislice-ct," Med. Data Anal. (ISMDA 2003, Berlin, Germany) ser. Lecture Notes in Computer Science, vol. 2868, Springer Verlag, Oct. 2003, pp. 77–84.

[18] K. Palagyi, E. Sorantin, E. Balogh, and A. Kuba, "A sequential 3D thinning algorithm and its medical applications," in *Proc. Inf. Process. Med. Imag. (IPMI 2001)*, Jun. 2001, vol. 2082, pp. 409–415.

[19] D. G. Morgenthaler, Three-Dimensional simple points: Serial erosion, parallel thinning and skeletonization Tech. Rep. TR-1005, 1981.

[20] H. Kitaoka, Y. Park, J. Tschirren, J. Reinhardt, M. Sonka, G. McLennan, and E. A. Hoffmann, *Automated Nomenclature Labeling of the Bronchial Tree in 3D-CT Lung Images*. Amsterdam, The Netherlands: Springer-Verlag, Oct. 2002, vol. 2489, Lecture Notes in Computer Science, pp. 1–11.

[21] A. Fitzgibbon, M. Pilu, and R. B. Fisher, "Direct least square fitting of ellipses," *IEEE Trans. Patt. Anal. Mach. Intell.*, vol. 21, no. 5, pp. 476–480, May 1999.

[22] W. R. Webb, N. L. Müller, and D. P. Naidich, *High-Resolution Ct of the Lung*. New York: Raven, 1992.

[23] C. Y. Seow, L. Wang, and P. D. Paré, "Airway narrowing and internal structural constraints," *J. Appl. Physiol.*, vol. 88, pp. 527–533, 2000.

[24] V. Brusasco and R. Pellegrino, "Complexity of factors modulating airway narrowing in vivo: Relevance to assessment of airway hyperresponsiveness," *J. Appl. Physiol.*, vol. 95, pp. 1305–1313, 2003.

[25] W. Schneider, T. Bortfeld, and W. Schlegel, "Correlation between ct numbers and tissue parameters needed for monte carlo simulations of clinical dose distributions," *Phys. Med. Biol.*, vol. 45, pp. 459–478, 2000.

[26] M. Hasegawa, Y. Nasuhara, Y. Onodera, H. Makita, K. Nagai, S. Fuke, Y. Ito, T. Besuyaku, and M. Nishimura, "Airflow limitation and airway dimensions in chronic obstructive pulmonary disease," *Am. J. Respir. Crit. Care Med.*, vol. 173, pp. 1309–1315, 2006.

[27] I. N. Bronstein and K. A. Semendjajew, *Taschenbuch Der Mathematik, 25. Auflage*. Berlin, Germany: Springer-Verlag, 1991.